Title

Localized strain profile in surface electrode array for programmable composite multiferroic devices

Journal

Applied Physics Letters, 118(18)

ISSN

0003-6951

Authors

Xiao, Zhuyun
Lai, Chelsea
Zheng, Ruoda
et al.

Publication Date

2021-05-03

DOI

10.1063/5.0039156

Peer reviewed

Localized Strain Profile in Surface Electrode Array for Programmable Composite Multiferroic Devices

Zhuyun Xiao[1,7], Chelsea Lai[1,7], Ruoda Zheng[2], Maite Goiriena-Goikoetxea[3, 4], Nobumichi Tamura[5], Cornelio Torres Juarez[2], Colin Perry[1], Hanuman Singh[3], Jeffrey Bokor[3], Gregory P. Carman[2], Rob N. Candler[1, 2, 6*]

1. Department of Electrical & Computer Engineering, University of California, Los Angeles, CA 90095, USA
2. Department of Mechanical & Aerospace Engineering, University of California, Los Angeles, CA 90095, USA
3. Department of Electrical Engineering and Computer Science, University of California, Berkeley, CA 94720, USA
4. Department of Electricity and Electronics, University of the Basque Country, Leioa 48940, Spain
5. Advanced Light Source, Lawrence Berkeley National Lab, Berkeley, CA 94720, USA
6. California NanoSystems Institute, Los Angeles, CA 90095, USA
7. Z. X. and C. L. contributed equally to this paper

* Email: rcandler@g.ucla.edu

Abstract:

We investigate localized in-plane strains on the microscale, induced by arrays of biased surface electrodes patterned on piezoelectrics. Particular focus is given to the influence that adjacent electrode pairs have on one another to study the impact of densely packed electrode arrays. We present a series of X-ray microdiffraction studies to reveal the spatially-resolved micron-scale strain distribution. The strain maps with micron-scale resolution highlight how the local strain

profile in square regions up to 250 × 250 μm^2 in size is affected by the surface electrodes that are patterned on ferroelectric single-crystal $Pb(Mg_{1/3}Nb_{2/3})O_3]_x$-$[PbTiO_3]_{1-x}$ (PMN-PT). The experimental measurements and simulation results show the influence of electrode pair distance, positioning of the electrode pair including the angle of placement, and neighboring electrode pair arrangements on the strength and direction of the regional strain. Our findings are relevant to the development of micro-architected strain-mediated multiferroic devices. The electrode arrays could provide array-addressable localized strain control for applications including straintronic memory, probabilistic computing platforms, microwave devices, and magnetic-activated cell sorting platforms.

Main Manuscript:

Using voltage-generated strain to control magnetism in miniaturized devices is an energy-efficient alternative to the conventional current-driven approach due to the Joule heating suppression. Such devices are based on a class of materials--magnetoelectric multiferroics. Recent advances in multiferroic magnetoelectric composites[1] have brought us closer to applying fundamental research discoveries to a broad range of applications, including data-storage devices[2–4], probabilistic computing platforms[5], voltage-tunable radio-frequency microwave devices[6,7], artificial neural networks[8,9], and microfluidic particle and cell sorting platforms[10–12]. For multiferroic heterostructures, understanding the strain that is coupled into the magnetoelastic structures is necessary, especially any variation in strain with length scales similar to the magnetic element size.

To date, researchers have extensively studied the electric-field control of magnetism in a variety of mechanically-coupled composite multiferroic heterostructures, where strain from a piezoelectric material[13–15] governs magnetism in an adjacent magnetoelastic material[16–18] due

to the converse magnetoelectric effect. To drive a desirable magnetoelastic response, instead of optimizing the material properties of magnetoelastic and piezoelectric constituents, one could use patterned surface electrodes to engineer the strain. With surface electrodes, the in-plane strain is generated locally between the electrodes, with the strain profile defined by the location and the orientation of the electrodes.

In this paper, we focus on examining the induced strain distribution in the single-crystal piezoelectric $Pb(Mg_{1/3}Nb_{2/3})O_3]_{0.69}$-$[PbTiO_3]_{0.31}$ (PMN-PT) with surface electrodes. As opposed to piezoelectrics fully covered with electrodes, which rely on piezoelectric coefficients d_{31}, d_{32} for in-plane anisotropic strain[19], the surface electrode design can provide more freedom in strain control due to the adjustability of the electrode arrangement. This work could serve as a roadmap/reference for designing compact, programmable electrode arrays for multiferroics applications.

Many multiferroic devices based on PMN-PT adopt a design that uses a single pair of electrodes across the entire surface. In particular, (011)-cut PMN-PT generates in-plane anisotropic strain to alter the magnetic domain in the coupled magnetic layer[20–23]. A tensile strain is induced along [01-1], and a compressive strain is generated along [100]. (001)-cut PMN-PT is another popular substrate choice, especially when the magnetic films require epitaxial growth, such as $La_{0.7}Sr_{0.3}MnO_3$ (LSMO)[24, 25] or $Fe_{(1-x)}Ga_x$ alloys[26], with a lattice match to PMN-PT[27]. With an applied electric field, the substrate typically undergoes isotropic, in-plane compressive strain[28,29]. Using this approach of a single pair of electrodes across the entire substrate, there is little control over the direction of strain, and no ability to individually control strain for different magnetic elements.

Alternatively, surface electrodes can be used to engineer the direction and magnitude of strain with local control. Surface electrode pairs patterned on piezoelectrics (PMN-PT[30], $Ba_{1-x}Sr_xTiO_3$ (BST)[7], PZT[31,32,33]) have shown local magnetoelectric control of Ni or FeGa elements[31, 32, 34]. These device prototypes have provided experimental evidence on the local strain-mediated behavior of a few micromagnets patterned between a set of electrode pairs a few hundreds of microns apart.

So far, little has been done to experimentally characterize the impact of neighboring electrode pairs on strain. In this work, we focus on characterizing the deviatoric strain (Supplementary Info S1) distribution between surface electrode pairs arranged in arrays on (001)-cut PMN-PT using synchrotron-based scanning X-ray microdiffraction[35]. The goal is to understand the role of electrode arrangement on the local strain distribution between the electrodes, which will provide insight into how densely electrode arrays can be packed while maintaining control of each magnetic element. We analyze the average local axial deviatoric strain along [100] and [010] directions, in the region between the surface electrode pairs. The local strain is compared with the axial strain generated by the parallel plate electrodes, which is expected to be compressive in-plane[28,29]. Furthermore, we examine the effect on strain from electrode pair arrangement and interactions among neighboring surface electrode pairs. Finite element simulations are used to better interpret the varied regional strain behavior.

In the experiment, the three (001)-cut PMN-PT samples (1 cm × 1 cm × 500 μm (thickness)), TRS Technologies, Inc., State College, PA, USA) under investigation are Sample A with parallel plate electrodes as a reference (Figure 1a), Samples B and C with 6 and 12 surface electrode pairs, respectively (Figure 1c). All of the electrodes consist of a 5 nm Ti and a 50 nm Pt layer. In Sample A, both the top and bottom surfaces are uniformly covered by an electrode.

For Sample B and C, arrays of electrode pairs are patterned on the top surface, while the bottom surface is covered uniformly by an electrode. The samples are wirebonded to leadless chip carriers (Figure 1c) before being mounted on to a printed circuit board.

Laue (polychromatic) X-ray microdiffraction can be used for investigating elastic strain distribution at the micron-scale[22,36–38] (Supporting Information S1). Recently, Lo Conte *et al.* used X-ray microdiffraction to map out the electrically-induced axial strain distribution in (011)-oriented PMN-PT with parallel plate electrodes[22], achieving micron-scale resolution at the locations with patterned magnetic microstructures (Figure 1a(i)). During the microdiffraction scanning, individual diffraction pattern is collected stepwise from a grid point (an x-y position) to provide information on lattice strain and crystal orientation. For this work, the electrically-induced deviatoric strain is calculated for each step, as represented by a 10×10 μm^2 pixel in the constructed 2D strain maps (Figure 1c), by taking the deviatoric strain difference of extracted strain at a non-zero voltage and at zero voltage. In Sample A, the X-ray performs a raster scan with an area of 500×500 μm^2 at the center of the sample. In Sample B and C, the X-ray scans multiple 250×250 μm^2 areas (Supporting Information S2). This work mainly focuses on the experimentally-measured in-plane deviatoric strain components[35], ε'_{xx} and ε'_{yy}, measured by Laue method, as they are the driving mechanism for in-plane magnetization rotation or switching in numerous studies[22,31,32,39]. In the remaining part of this paper, we will refer to deviatoric strain as strain.

Before examining the regional strain profile generated by the surface electrode pairs, we conduct X-ray microdiffraction on two prepoled PMN-PT samples with parallel plate electrodes and apply voltages up to 400 V (Supporting Information S3), as shown in Figure 1a. The first one (Figure 1a(i)), a (011)-cut PMN-PT studied in Lo Conte *et al*. generates in-plane

anisotropic strain along the main crystallographic directions [100] and [01-1] as a function of the voltage. The second one (Sample A, Figure 1a(ii)) is a (001)-cut PMN-PT, which would ideally exhibit isotropic compressive strain on a macroscopic level along the [100] and [010] directions[28,29]. For the first sample, the average induced in-plane strain is compressive along [100] and tensile along [01-1]. For the second, the average axial strains are both compressive. Interestingly, the axial strains between nominally equivalent [100] and [010] directions are close in magnitude but not identical when the strain is examined at the microscale. The error bars in the strain-voltage plot in Figure 1a also suggest that the axial strain exhibits spatial variation in the scanned regions for both PMN-PT samples. In Figure 1b, we show the difference between the average of two deviatoric strains as total (in-plane) strain from both samples. This difference is the driver for controlling magnetization (i.e., strain-induced magnetoelastic uniaxial anisotropy) in previously reported strain-coupled thin-film magnetic nanostructures[40,41]. For the (011)-cut PMN-PT, it is obvious that a large strain difference is induced at 400 V, whereas for the (001)-cut, the strain difference is much lower. Ideally, we expect this strain difference to be zero, but the local inhomogeneity of strain[22] and ferroelectric domains[18] likely account for the non-zero average in the biaxial strain difference magnitude.

Next, we obtain regional microdiffraction scans in Samples B and C for two voltage cycles from 0 V to 400 V, where the first one poles the samples (Supporting Information S3). During the microdiffraction experiment, a positive voltage is applied to the top surface electrodes, and the bottom is grounded (Figure 1c). The regions of interest are each marked by four markers and labeled numerically for ease of reference. Figure 1c (Right) also demonstrates the zoomed-in reconstructed deviatoric strain maps from Sample C. When a voltage is applied to the surface electrode pairs, to satisfy the compatibility conditions of strain[42], an in-plane compressive

strain is produced at the surface of the PMN-PT along the *y*-direction (i.e., the direction of the electrode pair), and a tensile strain is generated along the *x*-direction.

The major difference between samples B and C is the density of electrode array pairs, where C has two more rows of electrode pairs than B and thus is more densely packed, as shown in Figure 1c (Supporting Information S4). Two electrode pairs located at regions 3 and 12 in both samples share the same electrode pair configuration, where the electrode pairs are separated by 400 μm. Previous simulation studies have shown that at such a length scale, the surface electrode pair on a PZT could produce a highly localized strain field in regions smaller than 1 $\times$ 1 mm^2[31]. Since the separation distance between surface electrodes is on the order of a few hundred microns, it becomes impossible to characterize the strain by a strain gauge. Hence, X-ray microdiffraction is crucial for characterizing the spatial strain profile as a result of varied surface electrode array configuration, including pair density, separation distance between electrode pairs, and angle of the electrodes with respect to substrate crystallographic direction.

From X-ray microdiffraction data, we extract the electric-field induced deviatoric strains ε'_{xx} and ε'_{yy} for individual regions. Figure 2a shows an example of the 2D map of induced strain. As expected, the local induced strain is tensile along the *x*-direction and compressive along the *y*-direction. However, from the micron-scale mapping, the strain is not uniform at the micrometer scale. A finite element simulation using COMSOL Multiphysics (Supporting Information S5) with the same electrode setup as in Sample B also shows local anisotropic axial strain as in the experiment. The simulated induced strain mapping is shown in Figure 2a. For the simulation, we do not consider nonuniform strain and ferroelectric domains present in the experimental system, as suggested by the strain distribution in Sample A (Figure 1a(ii)), so the strain variation is less pronounced (Supporting Information S6).

To evaluate the experimental strain distribution and variation for the 625 pixels, we created violin plots[43] (Figure 2b) for both the axial deviatoric strains and their difference, ε'_{yy} - ε'_{xx}. To account for the experimental noise during X-ray microdiffraction scanning, apart from fitting Laue peaks with the XMAS software, we adopt the nearest neighbor technique for outlier removal (Supporting Information S7) with less than 0.6% of the pixels removed for any image. Additionally, we report the regional average strain in Figure 2c from both experiment and simulation. The differential deviatoric strain achieved in localized regions on (001)-cut PMN-PT using the surface electrodes in this work is similar to that of the global anisotropic strain profile in (011)-cut PMN-PT from Figure 1a(i). However, with the locally-controllable strain of our surface electrodes, one could, for example, actuate individual microscale magnetic components. Furthermore, the surface electrodes can be used to engineer the differential deviatoric strain, as opposed to the case of Figure 1a(i), which relies on having the appropriate material and crystalline cut, thus limiting the set of material choices.

Also observed from Figures 2b and 2c, the average strain for each direction and the strain difference vary by region. Such differences in local strain profile suggest a collective effect from the electrode pair separation distances (400 – 600 μm), the electrode pair rotation of 11.25^{o} in the bottom row and the location of the region in the sample. Next, we resort to simulation for providing additional insight on the effect of separation gap distance and angle using parametric sweeps. The simulation results in Figure 3a present the biaxial deviatoric strain difference as a function of electrode pair separation gap distance *d*. For the ranges studied experimentally, the simulations show decreasing strain in both *x*- and *y*- directions as the gap distance narrows. The corresponding axial strains measured experimentally for regions 1-3 in Sample B are marked in Figure 3a. In terms of the strain variation with electrode angles, an

increase in the electrode pair tilting angle with respect to the *x*-direction slightly decreases the strain along the [100] and [010] directions, as shown in Figure 3b.

We also compare the local strain results to the anisotropic axial strain generated globally in parallel plate (011)-cut PMN-PT substrate (Figure 1b). It is observed that the locally induced strain in the 6 regions (1-3, 10-12) are similar in magnitude as in the (011)-cut PMN-PT, a significant increase from the nearly isotropic compressive strain in Sample A with parallel plate electrodes.

We use axial deviatoric strain ratio[44] ($\varepsilon'_{yy}/\varepsilon'_{xx}$) to compare the strain behavior across different regions in a sample and similar regions across samples. Different ratios reflect variations in regional piezoelectric coefficients which allow one to access a diverse range of strain responses at a given applied voltage. First, we compare the axial strain ratio in all regions in Sample B (Supporting Information S6) to conclude that the strain is not strictly confined between electrode pairs; rather, it can affect the strain distribution outside of the region. Next, we compare the axial strain ratio to see how the variation of the electrode pair density affects the strain behavior in local regions. In particular, we compare the axial strain ratio in regions 3 and 12 from Sample B and C since those regions have identical electrode designs (i.e., same gap distance and angle). Similar to Sample B, the voltage-induced axial strain profile from prepoled Sample C (see Supporting Information S9) shows tensile and compressive strain along the *x*- and *y*- directions, respectively.

From both the experimental and simulation results (Figure 4), the $\varepsilon'_{yy}/\varepsilon'_{xx}$ ratio from Sample C is higher than that in Sample B. This observation implies that the presence of additional rows of electrode pairs in the middle in Sample C versus Sample B leads to a higher axial strain ratio.

It suggests the presence of denser electrode pairs along the *y*-direction plays a non-negligible role in making the regional strain profile more anisotropic along the *y*- versus *x*- directions. Overall, the X-ray microdiffraction results on the micron-scale level reveal that the local strain can be affected collectively by the three factors investigated in this work: local electrode separation distance, angle of placement with respect to the crystallographic directions, and closeness to neighboring electrodes. With the current surface electrode design, the samples generate localized strain with tunable axial strain magnitudes.

In conclusion, X-ray microdiffraction provides a distinct opportunity to map out the local deviatoric strain in ferroelectric PMN-PT in the areas of interest between surface electrodes with micron-scale resolution. An in-depth understanding of the spatial distribution of regional strain is crucial, particularly for driving arrays of strain-coupled magnetic microstructures in multiferroic systems. We characterize and analyze the strain profile in PMN-PT resulting from both parallel plate electrodes and patterned electrode arrays. The results highlight the effect of electrode geometry on both the local and global scales. In particular, we examined local strain in multiple regions from (001)-cut PMN-PT samples with surface electrodes, and the average axial strain response is consistent with predictions from piezoelectric simulations. This systematic study also highlights the influence of electrode pair geometry including separation distance of the pair, angle of the pair, and neighboring electrode pair compactness on local and regional strain.

Supplementary Material

The supplementary material contains more detail on the X-ray microdiffraction, experiment vs. simulation results, outlier removal for strain mapping, voltage-induced axial strain ratio, and information on strain variation among samples (Supporting Information S1-S9).

Acknowledgements

We gratefully acknowledge the support from the NSF Nanosystems Engineering Research Center for Translational Applications of Nanoscale Multiferroic Systems (TANMS) under the Cooperative Agreement Award No. EEC-1160504. We also acknowledge the use of the cleanroom service for device fabrication in the UCLA Nanolab at the University of California, Los Angeles. X-ray microdiffraction at the Advanced Light Source and fabrication at the Molecular Foundry were supported by the Office of Science, Office of Basic Energy Sciences, of the U.S. Department of Energy under Contract No. DE-AC02-05CH11231. M. G.-G. acknowledges the support of the Basque Government for the Postdoctoral Fellowship. The authors are very grateful to Jizhai Cui, Roberto Lo Conte, Camelia Stan, and Jinzhao Hu for their valuable discussions and to Arian Gashi for his support on fabrication at the Molecular Foundry. C. L., C. T. J., and C. P. acknowledge the support of the TANMS Undergraduate Research Program.

Data Availability

Raw data were generated at the Advanced Light Source, Berkeley National Lab. Derived data supporting the findings of this study are available from the corresponding author upon reasonable request.

References

[1] C.W. Nan, M.I. Bichurin, S. Dong, D. Viehland, and G. Srinivasan, J. Appl. Phys. **103**, 031101 (2008).

[2] M. Bibes and A. Barthélémy, Nat. Mater. **7**, 425 (2008).

[3] S. Manipatruni, D.E. Nikonov, and I.A. Young, Nat. Phys. **14**, 338 (2018).

[4] A.A. Bukharaev, A.K. Zvezdin, A.P. Pyatakov, and Y.K. Fetisov, Physics-Uspekhi **61**, 1175 (2018).

[5] M.T. McCray, M.A. Abeed, and S. Bandyopadhyay, Sci. Rep. **10**, 12361 (2020).

[6] W. Peng, B. Howe, and X. Yang, in *Integr. Multiferroic Heterostruct. Appl.* (2019), pp. 157–174.

[7] A.B. Ustinov, A. V. Drozdovskii, A.A. Nikitin, A.A. Semenov, D.A. Bozhko, A.A. Serga, B. Hillebrands, E. Lähderanta, and B.A. Kalinikos, Commun. Phys. **2**, 137 (2019).

[8] A.K. Biswas, J. Atulasimha, and S. Bandyopadhyay, Nanotechnology **26**, 285201 (2015).

[9] S. Boyn, J. Grollier, G. Lecerf, B. Xu, N. Locatelli, S. Fusil, S. Girod, C. Carrétéro, K. Garcia, S. Xavier, J. Tomas, L. Ballaiche, M. Bibe, A. Barthelemy, S. Saïghi, and V. Garcia, Nat Commun **8**, 14736 (2017).

[10] R. Khojah, Z. Xiao, M.K. Panduranga, M. Bogumil, Y. Wang, M. Goiriena-Goikoetxea, R. V Chopdekar, J. Bokor, G.P. Carman, R.N. Candler, and D. Di Carlo, Adv. Mater. 2006651 (2021).

[11] Y.C. Hsiao, R. Khojah, X. Li, A. Kundu, C. Chen, D.B. Gopman, A.C. Chavez, T. Lee, Z. Xiao, A.E. Sepulveda, R.N. Candler, G.P. Carman, D. Di Carlo, and C.S. Lynch, Appl. Phys. Lett. **115**, 082402 (2019).

[12] Z. Xiao, R. Khojah, M. Chooljian, R. Lo Conte, J.D. Schneider, K. Fitzell, R. V Chopdekar, Y. Wang, A. Scholl, J. Chang, G.P. Carman, J. Bokor, D. Di Carlo, and R.N. Candler, Multifunct. Mater. **1**, 014004 (2018).

[13] H. Uršič, M. Santo Zarnik, and M. Kosec, Smart Mater. Res. **2011**, 452901 (2011).

[14] P. Duran and C. Moure, Mater. Chem. Phys. **15**, 193 (1986).

[15] M. Acosta, N. Novak, V. Rojas, S. Patel, R. Vaish, J. Koruza, G.A. Rossetti, and J. Rödel, Appl. Phys. Rev. **4**, 041305 (2017).

[16] T. Wu, P. Zhao, M. Bao, A. Bur, J.L. Hockel, K. Wong, K.P. Mohanchandra, C.S. Lynch,

and G.P. Carman, J. Appl. Phys. **109**, 124101 (2011).

[17] J.J. Yang, Y.G. Zhao, H.F. Tian, L.B. Luo, H.Y. Zhang, Y.J. He, and H.S. Luo, Appl. Phys. Lett. **94**, 212504 (2009).

[18] Y. Ba, Y. Liu, P. Li, L. Wu, J. Unguris, D.T. Pierce, D. Yang, C. Feng, Y. Zhang, H. Wu, D. Li, Y. Chang, J. Zhang, X. Han, J. Cai, C.W. Nan, and Y. Zhao, Adv. Funct. Mater. **28**, 1706448 (2018).

[19] J. Ryu, J.E. Kang, Y. Zhou, S.Y. Choi, W.H. Yoon, D.S. Park, J.J. Choi, B.D. Hahn, C.W. Ahn, J.W. Kim, Y. Do Kim, S. Priya, S.Y. Lee, S. Jeong, and D.Y. Jeong, Energy Environ. Sci. **8**, 2402 (2015).

[20] Z. Xiao, R. Lo Conte, M. Goiriena-Goikoetxea, R. V. Chopdekar, C.H.A. Lambert, X. Li, A.T. N'Diaye, P. Shafer, S. Tiwari, A. Barra, A. Chavez, K.P. Mohanchandra, G.P. Carman, K.L. Wang, S. Salahuddin, E. Arenholz, J. Bokor, and R.N. Candler, ACS Appl. Mater. Interfaces **12**, 6752 (2020).

[21] H. Sohn, M.E. Nowakowski, C. Liang, J.L. Hockel, K. Wetzlar, S. Keller, B.M. Mclellan, M.A. Marcus, A. Doran, A. Young, M. Kla, G.P. Carman, J. Bokor, and R.N. Candler, ACS Nano **9**, 4814 (2015).

[22] R. Lo Conte, Z. Xiao, C. Chen, C. V. Stan, J. Gorchon, A. El-Ghazaly, M.E. Nowakowski, H. Sohn, A. Pattabi, A. Scholl, N. Tamura, A. Sepulveda, G.P. Carman, R.N. Candler, and J. Bokor, Nano Lett. **18**, 1952 (2018).

[23] M. Ghidini, R. Mansell, F. Maccherozzi, X. Moya, L.C. Phillips, W. Yan, D. Pesquera, C.H.W. Barnes, R.P. Cowburn, J.M. Hu, S.S. Dhesi, and N.D. Mathur, Nat. Mater. **18**, 840 (2019).

[24] H. Xu, M. Feng, M. Liu, X. Sun, L. Wang, L. Jiang, X. Zhao, C. Nan, A. Wang, and H. Li, Cryst. Growth Des. **18**, 5934 (2018).

[25] A. Herklotz, J.D. Plumhof, A. Rastelli, O.G. Schmidt, L. Schultz, and K. Dörr, J. Appl.

Phys. **108**, 094101 (2010).

[26] D. Seguin, M. Sunder, L. Krishna, A. Tatarenko, and P.D. Moran, J. Cryst. Growth **311**, 3235 (2009).

[27] O. Bilani-Zeneli, A.D. Rata, A. Herklotz, O. Mieth, L.M. Eng, L. Schultz, M.D. Biegalski, H.M. Christen, and K. Dörr, J. Appl. Phys. **104**, 054108 (2008).

[28] J. Irwin, S. Lindemann, W. Maeng, J.J. Wang, V. Vaithyanathan, J.M. Hu, L.Q. Chen, D.G. Schlom, C.B. Eom, and M.S. Rzchowski, Sci. Rep. **9**, 19158 (2019).

[29] C. Thiele, K. Dörr, O. Bilani, J. Rödel, and L. Schultz, Phys. Rev. B - Condens. Matter Mater. Phys. **75**, 054408 (2007).

[30] A. Kumar Biswas, H. Ahmad, J. Atulasimha, and S. Bandyopadhyay, Nano Lett. **17**, 3478 (2017).

[31] J. Cui, J.L. Hockel, P.K. Nordeen, D.M. Pisani, C. Liang, G.P. Carman, and C.S. Lynch, Appl. Phys. Lett. **103**, 232905 (2015).

[32] H. Sohn, C. yen Liang, M.E. Nowakowski, Y. Hwang, S. Han, J. Bokor, G.P. Carman, and R.N. Candler, J. Magn. Magn. Mater. **439**, 196 (2017).

[33] C. Chen, J. Sablik, J. Domann, R. Dyro, J. Hu, S. Mehta, Z. Xiao, R. Candler, G. Carman, and A. Sepulveda, J. Phys. D. Appl. Phys. **53**, 174002 (2020).

[34] C.Y. Liang, S.M. Keller, A.E. Sepulveda, W.Y. Sun, J. Cui, C.S. Lynch, and G.P. Carman, J. Appl. Phys. **116**, 123909 (2014).

[35] N. Tamura, in *Strain Dislocation Gradients from Diffr. Spat. Local Struct. Defects*, edited by R. Barabash and G. Ice (Imperial College Press: London, 2014), pp. 125–155.

[36] N. Tamura, A.A. MacDowell, R. Spolenak, B.C. Valek, J.C. Bravman, W.L. Brown, R.S. Celestre, H.A. Padmore, B.W. Battermsan, and J.R. Patel, J. Synchrotron Radiat. **10**, 137 (2003).

[37] P.A. Lynch, A.W. Stevenson, D. Liang, D. Parry, S. Wilkins, and N. Tamura, Rev. Sci.

Instrum. **78**, 023904 (2007).

[38] M. Goiriena-Goikoetxea, Z. Xiao, A. El-Ghazaly, C. V. Stan, J. Chatterjee, A. Ceballos, A. Pattabi, N. Tamura, R. Lo Conte, F. Hellman, R. Candler, and J. Bokor, Phys. Rev. Mater. **5**, 24401 (2021).

[39] Z. Xiao, R. Lo Conte, C. Chen, C.Y. Liang, A. Sepulveda, J. Bokor, G.P. Carman, and R.N. Candler, Sci. Rep. **8**, 5207 (2018).

[40] M. Buzzi, R. V. Chopdekar, J.L. Hockel, A. Bur, T. Wu, N. Pilet, P. Warnicke, G.P. Carman, L.J. Heyderman, and F. Nolting, Phys. Rev. Lett. **111**, 027204 (2013).

[41] R. Lo Conte, Z. Xiao, C. Chen, C. V. Stan, J. Gorchon, A. El-Ghazaly, M.E. Nowakowski, H. Sohn, A. Pattabi, A. Scholl, N. Tamura, A. Sepulveda, G.P. Carman, R.N. Candler, and J. Bokor, Nano Lett. **18**, 1952 (2018).

[42] A.R. Bishop, T. Lookman, A. Saxena, K. Rasmussen, and S.R. Shenoy, Phys. Rev. B - Condens. Matter Mater. Phys. **67**, 024114 (2003).

[43] Jonas, MATLAB Cent. File Exch. (2020).

[44] T.H. Topper, J.J.F. Bonnen, M. Khalil, and A. Varvani-Farahani, J. Mater. Sci. **46**, 215 (2011).

Figure Captions

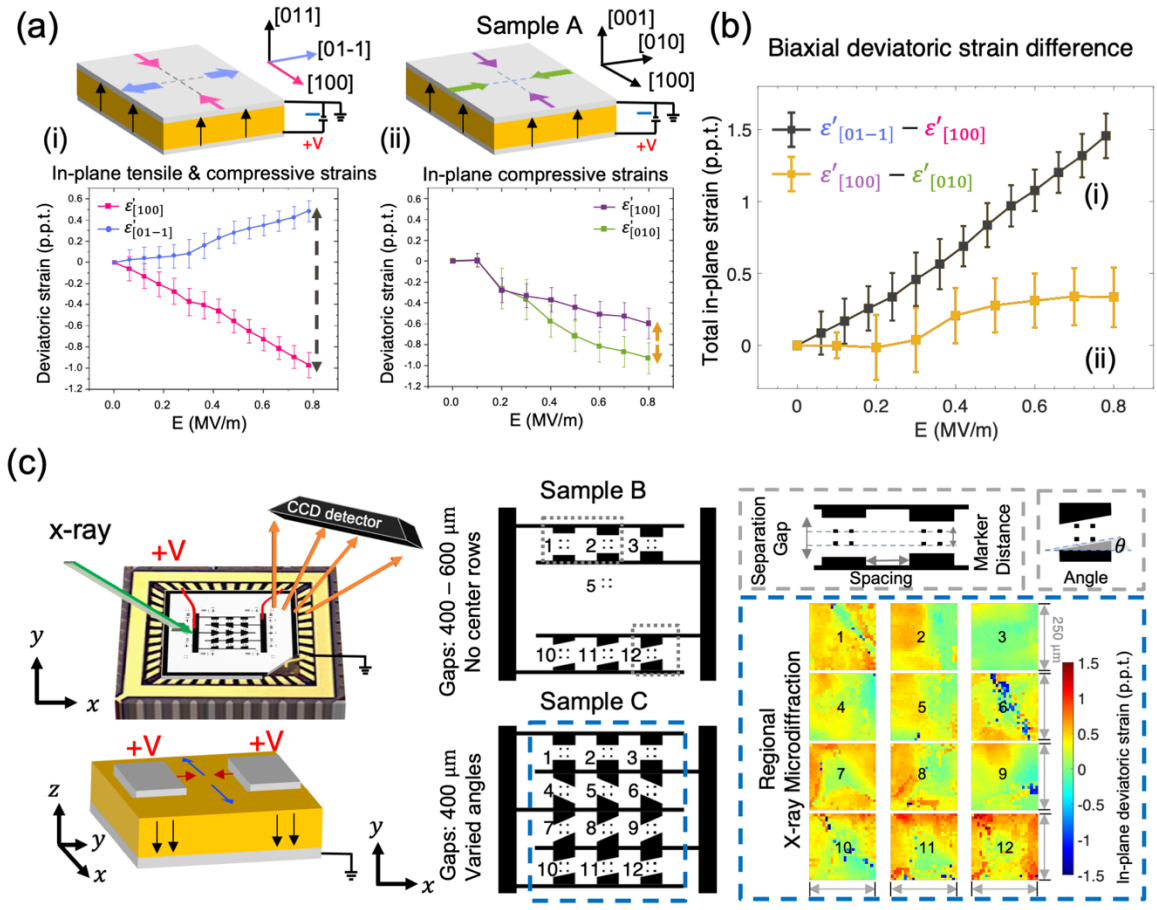

FIG. 1. (a) Schematics of PMN-PT with parallel-plate electrodes. (i) (top) (011)-cut exhibits a strong in-plane anisotropic strain; (bottom) X-ray microdiffraction results confirm the presence of a negative compressive deviatoric strain along [100] and a positive tensile deviatoric strain along [01-1] when voltage is applied. (ii) (top) (001)-cut with in-plane compressive strains when voltage is applied; (bottom) X-ray microdiffraction results show compressive deviatoric strain along both [100] and [010] directions. (b) Total in-plane strain (difference between deviatoric strains in the directions highlighted in (a)) vs electric field. Error bars represent the standard deviation of the pixel-wise micron-scale strain. (c) Schematics of X-ray

microdiffraction with *in situ* voltage applied. Surface electrode arrays on (001)-cut PMN-PT. Samples B and C have varied electrode pair distances, spacing and angle arrangements. In each region, four dot squares serve as location reference points. (Right) A demonstration of the reconstructed regional strain maps (ε'_{xx}) of the 12 dotted regions from Sample C.

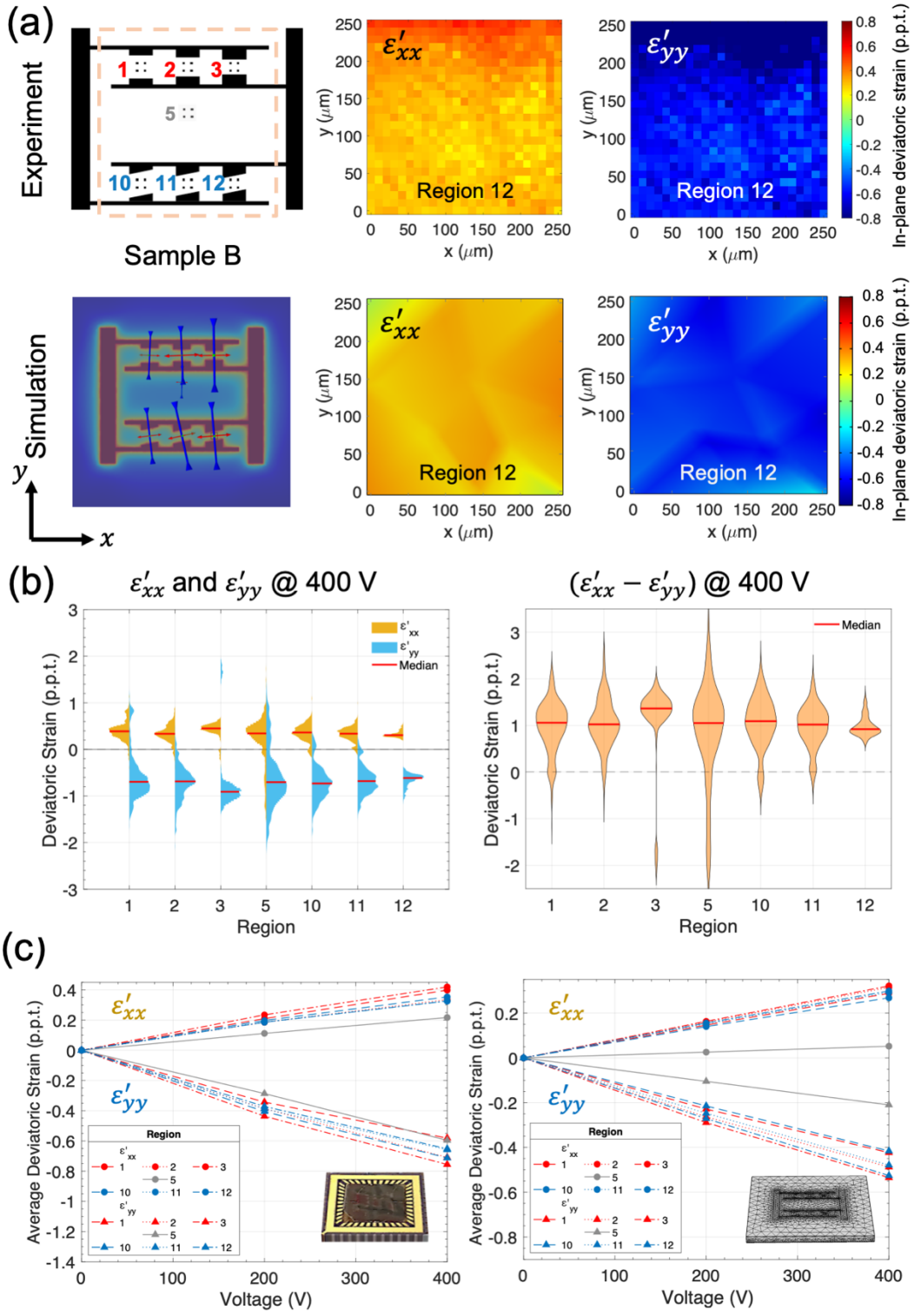

FIG. 2. (a) X-ray microdiffraction scans are conducted locally with an area of 250 × 250 μm^2 in 7 regions on Sample B. The electrode gap distance decreases from 600 to 400 μm in 100 μm decrements for regions 1-3, and 10-12. Reference region 5 is outside of the individual electrode

pairs. (Top) 2D strain map for region 12, in both x- and y- directions. Each pixel has a size of $10 \times 10\ \mu m^2$. (Bottom) Simulation results. (b) Violin plot with the distribution of (Left) the induced strains along x- and y- directions (ε'_{xx} and ε'_{yy}, respectively) and (Right) the in-plane biaxial strain difference. (c) Average axial strain vs. voltage for all regions in Sample B (Left) from experiment and (Right) simulation.

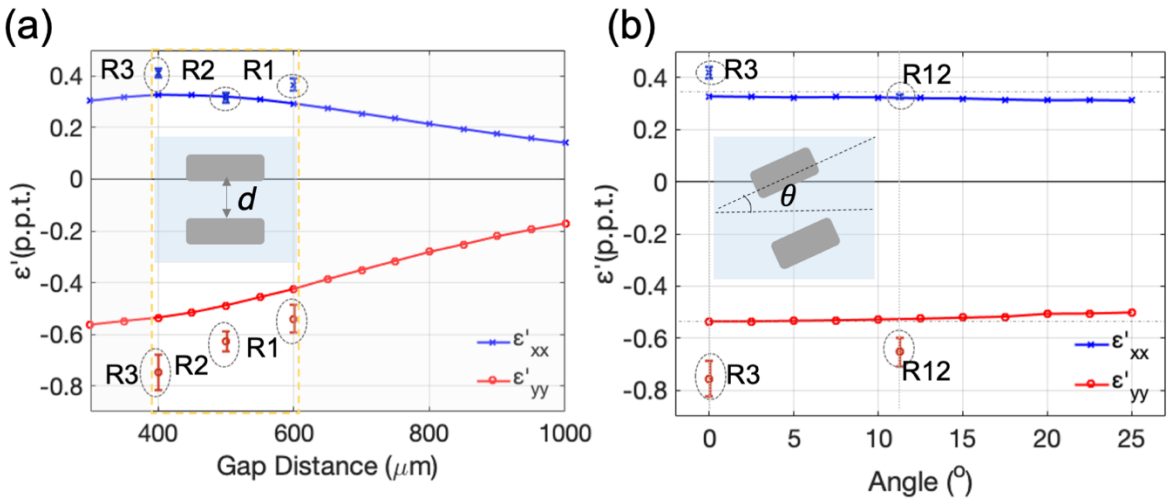

FIG. 3. A parametric sweep study using finite element simulation shows the effect on the induced deviatoric strain from electrode gap distance and angle. Corresponding average strain values obtained experimentally from regions 1-3 (labeled R1-R3, respectively) in Sample B are highlighted in circles with error bars representing 95% confidence intervals. (a) Gap distance between the electrode pairs affects the axial strain magnitudes. For the range explored experimentally, an increase in gap distance leads to a decrease in strain (highlighted by a dotted circle). (b) Role of electrode angle (with respect to the [010] crystallographic direction). In Sample B, as the angle increases from 0° to 11.25°, the deviatoric strains decrease slightly.

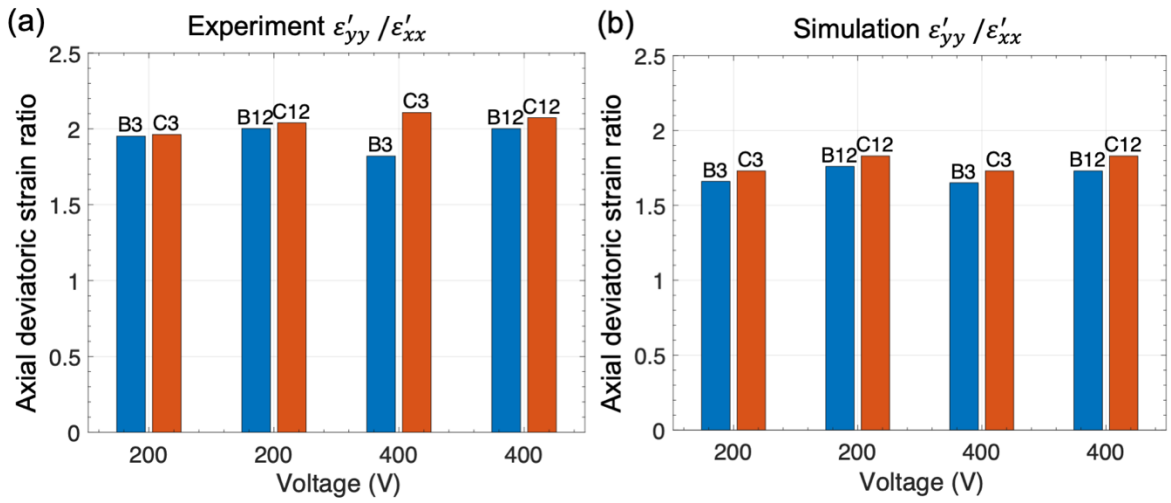

FIG. 4. Comparison of axial deviatoric strain ratios $\varepsilon'_{yy}/\varepsilon'_{xx}$ in regions 3 and 12 at 200 V and 400 V. From both (a) experiment and (b) simulation results, the ratios are higher in both regions from Sample C than those from Sample B, implying the additional electrodes in sample C couple with their neighbors and lead to increased anisotropic strain.